

**TEMPORAL AND SPATIALLY RESOLVED PARTICLE SIZE AND SPEED MEASUREMENTS IN
SUBSONIC AND TRANSONIC TURBOMACHINES**

Ilias Bosdas¹ Michel Mansour¹ Anestis I. Kalfas² Reza S. Abhari¹

¹ Laboratory for Energy Conversion, Department of Mechanical and Process
Engineering, ETH Zurich, Switzerland

² Department of Mechanical Engineering, Aristotle University of
Thessaloniki, 54124 Thessaloniki, Greece

Abstract

Aircraft engines are often operated in harsh environments allowing large particles, such as volcanic ash, ice and water droplets, to enter the flow path causing significant damages and malfunctions of the gas turbines. The current paper presents a unique set of experimental data measured with a novel optical backscatter probe capable of measuring coarse particle inside the flow path of a gas turbine. The measurements were conducted in an axial turbine test facility equipped with an in-house coarse water droplets spray generator. The measurements were performed under two different operating conditions at two different axial locations downstream of the stator's trailing edge. The measurements show that the coarse droplets' concentration is high at the stator trailing edge due to water film tearing. The measurements also show that the part load condition results in larger droplet diameters and higher relative droplet speeds. As a consequence higher erosion rates at the rotor leading edge suction side will occur when operating at part load condition.

Nomenclature

c	stator's chord	[mm]
x	stator's axial downstream location	[mm]
D	diameter	[μm]
t	time	[sec]
U	velocity	[m/s]

T	Temperature	[K]
fg	droplet frequency generator	[kHz]
We	Weber number	[-]
R	Erosion Rate	[-]
MF	Mass flow	[kg/s]

Greek:

λ	wavelength	[μm]
σ	surface tension	[N/m]
ρ	density	[kg/m^3]
ω	rotational speed	[rad/s]

Subscripts:

res	residence
eff	effective
avg	average value
10	arithmetic mean diameter
32	Sauter mean diameter
M	most frequent value in a data set (i.e diameter)
abs	absolute
rel	relative
f	flow
d	droplet
e	erosion

Introduction

Aircraft engines are often operated in hostile environments that cause significant amount of fine particulate matter, such as sand or volcanic ash, to penetrate into the gas turbine flow path. These particles result in blade erosion, aerodynamic disturbances, compressor instabilities and many times in total engine failure. The recent volcanic eruption in Iceland in April 2010 brought special attention to the problem of

particle measurements in the flow path of an aircraft engine. More than 100,000 flights were cancelled during an 8-day period due to safety reasons, accounting for 48% of total air traffic and roughly 10 million passengers. In that regard extensive experimental work has been performed in [1-3] mainly focused on ash deposition on turbine blades that causes malfunctions of the secondary air cooling system. Researchers have shown that gas temperature has a first order effect on deposition growth of the ash in turbine blades and volcanic ash can cause severe damage to the high pressure turbine components as well as to the combustor.

Atmospheric ice and subcooled water ingestion due to severe weather conditions has as well negative effects on engines' performance. The ice tends to accumulate on the compressor's blades changing their aerodynamic performance due to altered shape and roughness. It is therefore important to predict the amount and location of ice accretion to predict the loss of performance and prevent the risks of compressor stall and surge. In that regard, a substantial effort to understand and model the ice particles trajectories has been reported in [4-7] mainly concentrated in numerical simulations with the lack of experimental data for models validation.

Another field that involves particle's motion in the gas turbine's flow path is wet compression. Wet compression technique has been investigated extensively due to increase on gas turbine performance by lowering compressor's inlet temperature. However, this technique could have a negative effect as well by lowering the aerodynamic efficiency and narrowing efficiency peak [8]. The high bypass turbofan designs since 1970s, have increased significantly the propulsion efficiency of the aero-engine and

as result this technology was abandoned by that time. Nevertheless it is still utilized at stationary gas turbines due to the benefits mentioned before. Nowadays, the high need for more efficient and powerful aircraft engines has brought again the technology under investigation. As described in [9] short time water injection in the compressor or the combustor would increase the thrust (wet thrust) during aircraft starting at high altitude airports and/or high ambient temperatures. In civil aviation experimental and numerical results indicate that water injection has great influence on compressor performance, resulting in mass flow and pressure ratio changes [10]. Nevertheless, the droplet diameter distribution and concentration are essential information for the model's boundary conditions in order to investigate potential droplets' evaporation or damage due to blade erosion. The lack of experimental data for numerical models validation is more than obvious and consists an important drawback for further development of the current technique.

As described in this paragraph, it is clear that the presence of particles in the flow path of a gas turbine can result in undesirable engine's operation. In order to improve their efficiency and reliability, the flow mechanisms that dominate particle motion need to be understood and correlated to the main engine's operating flow field. The flow interactions between stationary and rotating blade rows generate a highly unsteady three-dimensional flow, which makes time resolved measurements very challenging. The current paper presents the results from a novel fast response optical probe for particle measurements (FRAP-OB) developed in LEC lab at ETH [11]. The study is focused on droplet measurements downstream of the stator of a one and half stage axial turbine test facility (LISA)

for two different operating conditions. In order to analyze the particle interactions with the flow field and the downstream rotor, time resolved aerodynamic measurements have been additionally performed.

Measurement technology

In the current study a newly developed optical backscatter probe for coarse water droplet measurements is used. The probe design and operating principle are described in detailed by Bosdas et al. in [11]. This probe has an embedded high bandwidth miniature photodiode capable of measuring particle speeds up to $Ma=0.5$. The probe tip is 5.5mm in diameter and the measurement range of the droplet diameters is from 45 up to 110 μm . As shown in Figure 1, light is guided in the probe tip through an optical fiber and then it is focused three probe diameters far from the tip forming the measurement sample volume.

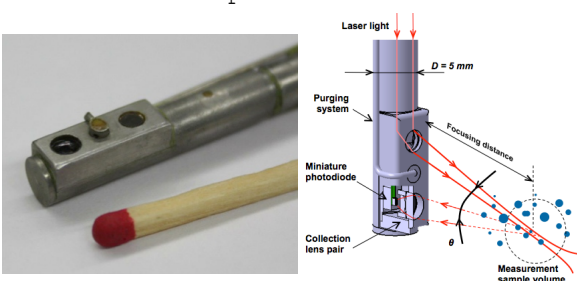


Figure 1: FRAP-OB probe tip with purging interface for windows protection

For this purpose a monochromatic ($\lambda=632\text{nm}$) He-Ne laser is used. When the particles cross the focused sample volume, they scatter light in all directions, but the installed photodiode captures the scatter light at specific backscatter solid angle through a set of collective lenses. In addition, the probe tip is equipped with a purging system in order to maintain the windows clean from water. This active system helps to maintain the laser beam of the

probe straight as it exits the optical window and avoid any beam deflection due to water contamination on the windows surface. The purging flow is attached to the surface of the windows in order to minimize any interaction with the surrounding flow field.

The FRAP-OB is calibrated in a monodispersed calibration facility as described in [11]. The probe calibration is performed using an in-house droplet generator developed by Rollinger et al. [12]. Monodispersed droplet generation in the kHz range is based on the Rayleigh breakup jet. For the current work the device was tuned to produce monodispersed water droplets with an accuracy of $\pm 2\mu\text{m}$ in diameter that are generated continuously with a frequency and air-backpressure set by the user.

For independent reference measurements of the droplet size the shadow imaging technique was utilized. The droplets are imaged with a high resolution camera that is triggered with a strobe light in order to capture images of the generated droplets. The droplet generator was tuned to generate monodispersed water droplets from 45 to 110 μm in diameter with steps of about 10 μm . In a second step, the droplet diameter is obtained counting the number of pixels of each image and multiplying it with the camera's pixel size. For the maximum amplification factor the accuracy of this technique results in an error of $\pm 0.69\mu\text{m}$ in diameter. The calibration of FRAP-OB probe is completed when the probe's output voltage signal is correlated with the measured droplets' diameter from the pictures. As shown in Figure 2, the calibration curve is modeled by an exponential curve fit.

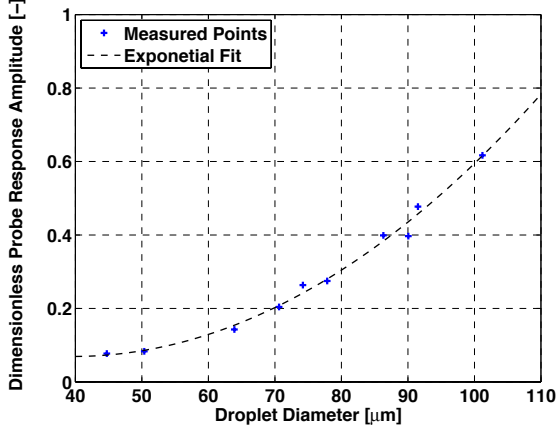


Figure 2: FRAP-OB calibration curve created with monodispersed water droplets

In addition, the probe was calibrated for droplet speed measurements. The velocity of the droplets during calibration procedure was measured via the generated pictures using Eq. (1).

$$U = \lambda \times fg \quad (1)$$

where λ is the actual distance between two consequent water droplets and fg is the frequency of the generated droplets set by the frequency generator. After calculating the velocity U and the residence time t_{res} , the time that one droplet needs to cross the measurement volume of the FRAP-OB, the effective beam diameter of the probe's sample volume can be calculated using Eq. (2).

$$D_{eff} = U \times t_{res} \quad (2)$$

In order to calculate the real velocity in an environment where the droplet's speed is unknown, the effective beam diameter as presented in Figure 3 is divided with the measured residence time t_{res} that is obtained from the FRAP-OB raw signal.

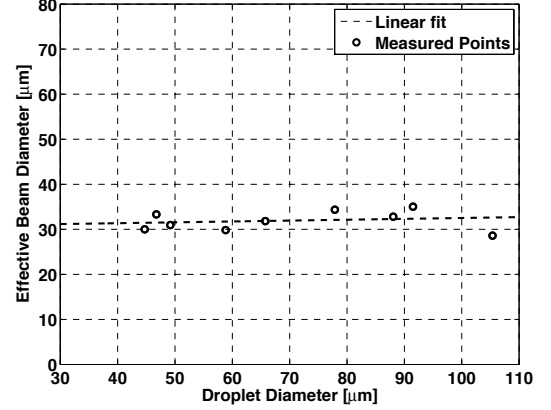


Figure 3: Effective beam diameter as a function of droplet diameter obtained from the FRAP-OB calibration procedure

Post processing code description

For the novel measurement system a post-processing algorithm consisting of multiple filtering and detections functions was developed to derive the droplets' size. A flow chart of the post-processing algorithm is presented in Figure 4. As mentioned previously, the FRAP-OB probe is a single particle detector, which implies that every droplet that crosses the sample volume of the probe will generate an output voltage signal. Since the backscatter signal amplitude from small droplets is at least three to four orders of magnitude lower than the respective forward scattering signal and the probe's bandwidth was kept high to allow measurements with high droplet velocities, the signal to noise ratio is a challenging subject. In order to cope with it, the processing algorithm applies a high pass filter to detect the droplets' peak location and a low pass filter to generate the dynamic offset that is generally affected by external low frequency noise. In a second step, the pulse amplitude that is a function of the droplet diameter is retrieved by subtracting the peak height from the dynamic offset for each time step peak location. The

pulse width is correlated to the droplet velocity according to the calibration of the effective beam diameter as described previously.

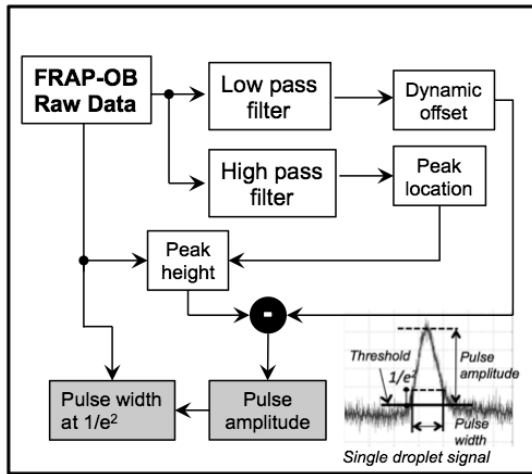


Figure 4: FRAP-OB post processing flow chart

Experimental Set up

The experimental study was carried out in the research axial turbine facility "LISA" in the Laboratory for Energy Conversion at ETH Zurich. The one-and-a-half stage, unshrouded, highly loaded axial turbine with 3D blading is a representative of modern high-pressure aircraft gas turbine. The research turbine facility consists of a quasi-closed air loop, which includes a single stage radial compressor, a two stage water-to-air heat exchanger and a calibrated venturi nozzle for accurate mass flow measurements. Upstream of the turbine test section there is a 3m long flow conditioning stretch in order to ensure a homogenous flow field. A DC generator absorbs the turbine's power and controls the rotational speed with an accuracy of $\pm 0.02\%$ (± 0.5 rpm). The water-to-air heat exchanger controls the inlet total temperature $T_{tot,in}$ to $\pm 0.3K$. The compressor ratio can be regulated in order to operate in design speed or part load conditions. A schematic of the experimental facility is shown in Figure 5.

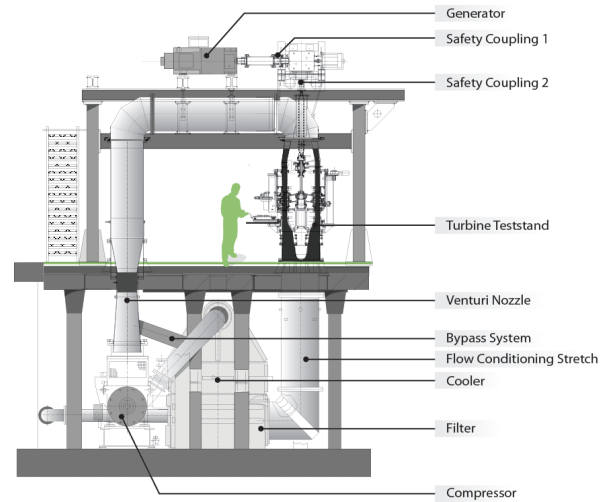


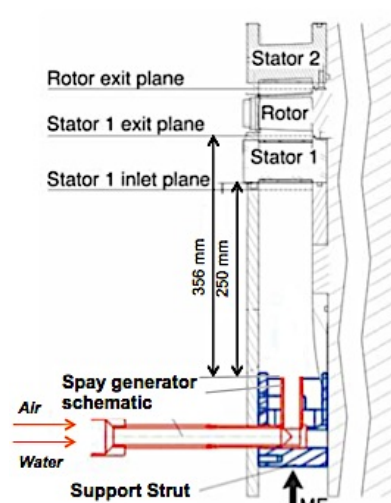
Figure 5: Schematic of LISA turbine test facility

For the present measurements, the facility was equipped with a 1.5 stage of an axial turbine that is described in Behr et al. [13]. Two operating conditions were studied, one at nominal operating design point and one at part load to investigate the droplet formation at reduced relative flow velocities. The rotor rotational speed for all operating conditions was kept constant at 2700rpm, which corresponds to a rotor blade passing frequency of 2430Hz. The FRAP-OB results presented in this paper were made at two axial downstream locations from the trailing edge of stator 1, one at 2% and the second at 8%. The measurement grid is comprised of 21 points in the radial direction, and 20 equally spaced traverses in the circumferential direction that cover 1 stator pitch (10°). The data were acquired at a sampling rate of 62.5 MHz over a period of 320 msec. The main operating parameters and conditions are summarized in Table 1.

Table 1: Operating conditions and geometrical characteristics

	Design point	Part load
Rotor Speed [RPM]	2700	2700
Rotor/Stator Blades	54/36	54/36
Rotor Blade Passing Freq [Hz]	2430	2430
Pressure Ratio 1.5-Stage, tot-st	1.65	1.33
Turbine Entry Temperature [°C]	55	55
Total Inlet Pres. [bar abs norm]	1.4	1.2
Stator 1 Exit Mach number (avg)	0.52	0.42
Stator 1 Exit Flow Angle [deg]	73.1	72.8
Mass Flow [kg/s]	12.13	8.4
Shaft Power [kW]	288	132
Hub/Tip diam. [mm]	660/800	660/800

A custom-made water spray generator was installed 5 stator chords upstream of the test section. The current droplet generator is capable to generate a spray with droplet diameters from 1 to 200 μ m covering one and half stator passage and injecting at mid-span location with a mass flow of 0.16lt/min. The spray generator was embedded in a support strut with a standard NACA 0012 profile to create an aerodynamic shape and minimize any interactions of the injector body with the generated water spray and airflow. Measurements were performed at the inlet plane as well as the stator 1 exit plane for the two different operating conditions. A schematic of the test section region with the custom-made droplet generator are shown in Figure 6.

**Figure 6: Cross section of the test segment (Turbine Teststand)**

Results and discussion

Results for design and part load conditions at the location of $x/c=2\%$

In this paragraph the design and part load operating conditions results at $x/c=2\%$ downstream of stator 1 (Figure 6: Stator 1 exit plane) are presented. As shown in Figure 7.a all droplets above 45 μ m in diameter are located at the stator's trailing between 20 and 85% in the spanwise direction covering approximately 20% pitch in circumferential direction. Figure 8 shows the time-averaged results of the Mach number downstream of the same stator. The stator wake and therefore the location of the trailing edge can be identified at 0° pitch from 0 to 100% span. In the same figure one can locate the hub and tip passage vortices located on stator's suction side between 0 and +0.25 pitch at 10% and 85% span respectively. In all plots the observer looks upstream. The results of Figure 7.a imply that coarse droplets are impacting the suction side of the stator and create a film of water on its surface. As a result they exit the stator trailing edge with significant lower velocity compared to the flow field velocity as it

will be shown in the next paragraphs. The same behavior is observed in Figure 7.b but with a wider circumferential coverage (25% pitch) and a small migration towards the center of the blade span.

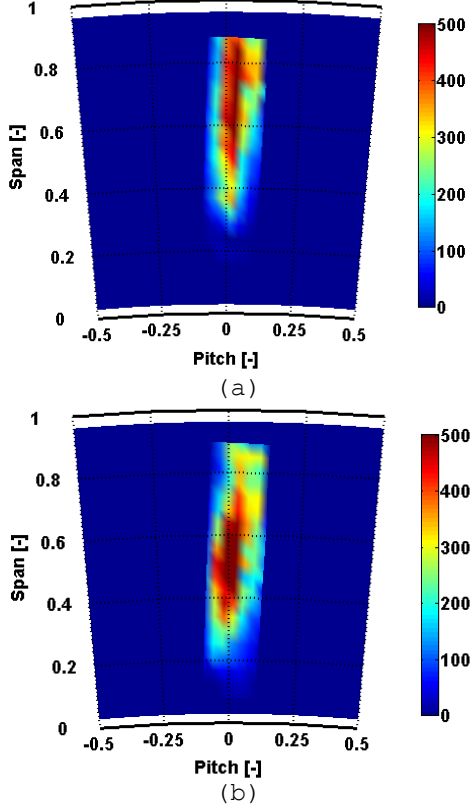


Figure 7: Droplet rate [droplets/rev] at Stator 1 exit plane for design point (a) and part load condition (b). Observer looks upstream.

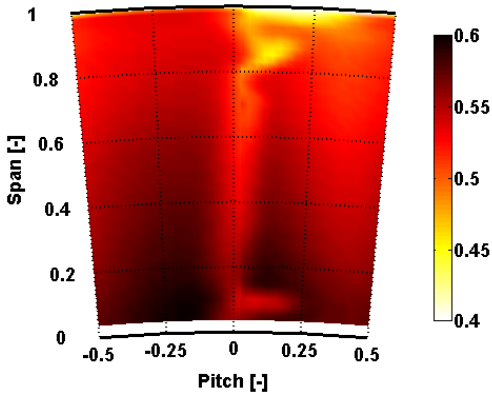


Figure 8: Absolute Mach number [-] at Stator 1 exit plane for design operating condition. Observer looks upstream

In order to analyze and understand the difference in droplet size and location, the droplet size distribution is investigated at three distinct blade span locations, the hub, mid and tip region at 25, 50 and 75% blade span respectively. Figure 9 summarizes the droplets' size distribution related to the two measured conditions. Each plot contains the droplet Sauter mean diameter, Mode value of the diameter as well as the mean value of the distribution. The droplet size distribution follows a skewed normal distribution for all cases. As depicted in Figure 9, two main observations emerge. The first is the reduction of the droplet size, by shifting the distributions to the left, with the increase of the relative flow velocity from part load to design speed. The Sauter Mean Diameter is reduced by 8%, 10% and 10.5% for the tip, mid and hub span locations respectively when the absolute Mach number increases from 0.42 to 0.52. The second observation is the increase of droplet's diameter from hub to the blade tip region. In this case, the Sauter Mean Diameter has increased by 10.3% and 8% for the design and part load conditions respectively. In order to explain these trends, the Weber number as expressed in Eq.(3) is used. The Weber number is defined as the ratio of the dynamic to the surface-tension force acting on a drop and it is a measure of the droplet stability for i.e the ability of the droplet to maintain a spherical geometry while shear forces try to tear it apart.

$$We = \frac{D \cdot \rho_f \cdot |U_d - U_f|^2}{\sigma_d} \quad (3)$$

When $We \ll 20$ the droplets are spherical and stable in size. As the Weber number increases above the value of 20 to 23 the droplets begin to deform and break up into smaller sizes [14, 15]. Following this theoretical analysis on the current results, one can say that the principal cause for the

reduction on the droplet size from part load to the design operating condition is due to the increase of $|U_d - U_f|^2$ term in Eq. (3). As consequence higher shear forces between the flow and the droplets are generated which lead to greater values of Weber numbers resulting in larger droplets' break up.

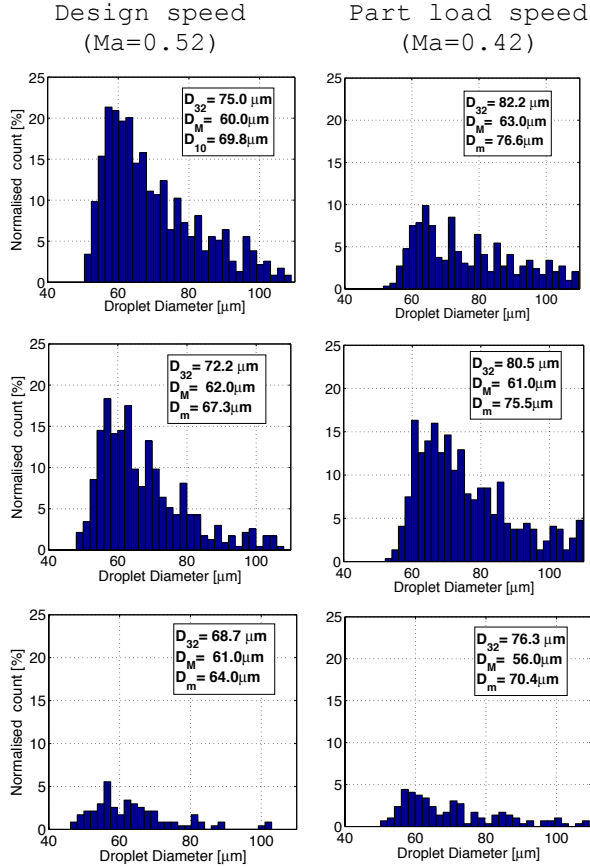


Figure 9: Size droplet distribution at tip (upper), midspan (center) and hub (bottom) spanwise locations for design and part load conditions at $x/c=2\%$ downstream of stator 1 exit

The lower mean flow velocities at the tip region, on an average by 8% as shown in Figure 10 and locally by 18% as shown in Figure 8, result on smaller values of We number and therefore on larger droplet diameters. This can explain the second observation where the droplet diameters are larger in the tip region of blade span compared to the hub span location.

Additional aerodynamic results for the design operating condition can be found in [13].

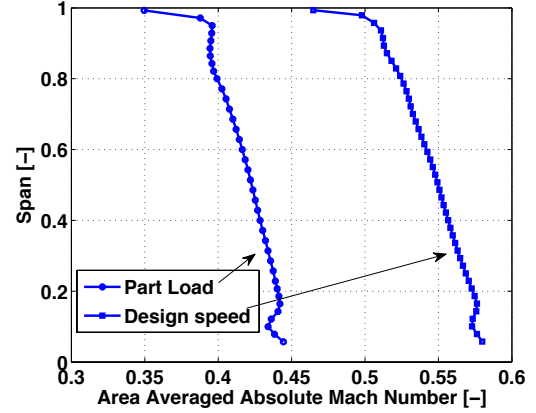


Figure 10: Area averaged absolute Mach number for design and part load operating conditions at Stator 1 exit plane.

Many research studies address the significance of the droplet velocity magnitude relative to the rotor tip speed velocity [16-18]. This is due to the fact that erosion rate on rotor blades is proportional to the droplet velocity and momentum described with a power law equation $R_e \sim U^n$, where n is between 3-5 [17, 18] and is a factor which is material dependent. Figure 11 shows a schematic of the velocity triangles at stator 1 exit plane. As depicted in Figure 11, the absolute droplet velocity ($U_{d,abs}$) is assumed to have the same exit angle as the main absolute flow field angle ($U_{f,abs}$) [19]. Following this assumption, the droplet relative velocity ($U_{d,rel}$) can be calculated through the rotor rotational velocity ($U = \omega r$) for each radial location. The time averaged absolute flow yaw angle velocity is 73.1° and 72.9° for design and part load conditions respectively.

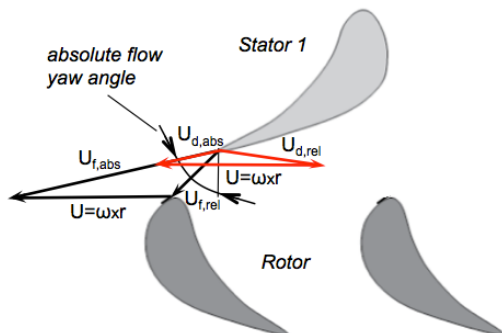
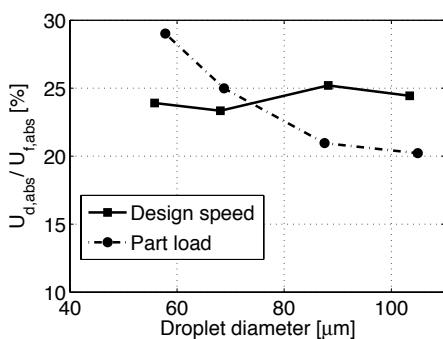
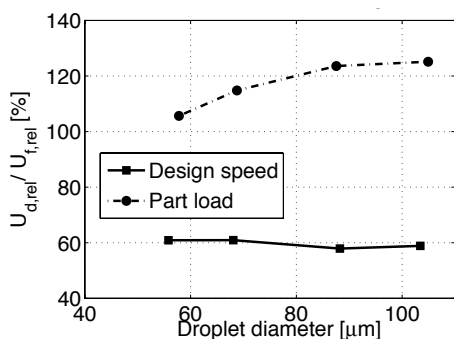


Figure 11: Velocity triangles flow field (black) and droplets (red) at stator 1 exit



(a)



(b)

Figure 12: Absolute (a) and relative (b) droplet velocity at midspan location for design and part load conditions

Results of Figure 12.a show that for both operating conditions the droplets ranging from 55 up to 100μm diameter have on an average a deficit of 80% in absolute velocity compared to the flow. Therefore the large water droplets will impact the rotor blade on the suction side of the leading edge. On the other

hand Figure 12.b shows that the droplets' relative velocity is on an average 2 times larger for part load condition compared to design operating point. At part load condition the droplets in the range of 50μm in diameter have approximately the same relative velocity as the flowfield relative velocity ($U_{d,rel} \sim U_{f,rel}$) and the droplets at the range of 100μm have 20% higher relative velocity compared to the flowfield relative velocity for the part load condition. For the design operating point there is no dependency of the relative droplet velocity with the droplet size and the relative droplet velocity is 40% lower compared to the part load condition as shown in Figure 12.b. The droplets will further accelerate, due to aerodynamic drag forces, and reach a maximum velocity depending on the available axial gap between stator and rotor blades [18, 20]. In order to further understand the formation mechanisms and be able to assess the droplets' maximum velocity before impacting the rotor leading edge additional measurement were performed at a second downstream location of stator 1.

Results for part load condition at locations of $x/c=2\%$ and 8%

Since part load conditions have greater impact on the erosion mechanisms as shown in Figure 12.b, results only from this operating point are presented in this paragraph for two different axial locations downstream of Stator 1. As shown in Figure 13, the droplet size reduces significantly while they accelerate from the stator trailing edge towards the rotor leading edge. This is expressed by the reduction on the actual value of the diameter as well as the reduction in detected coarse droplet count. The Sauter Mean Diameter has been reduced by 10%, 11.3% and 3% for the tip, mid and hub span locations respectively.

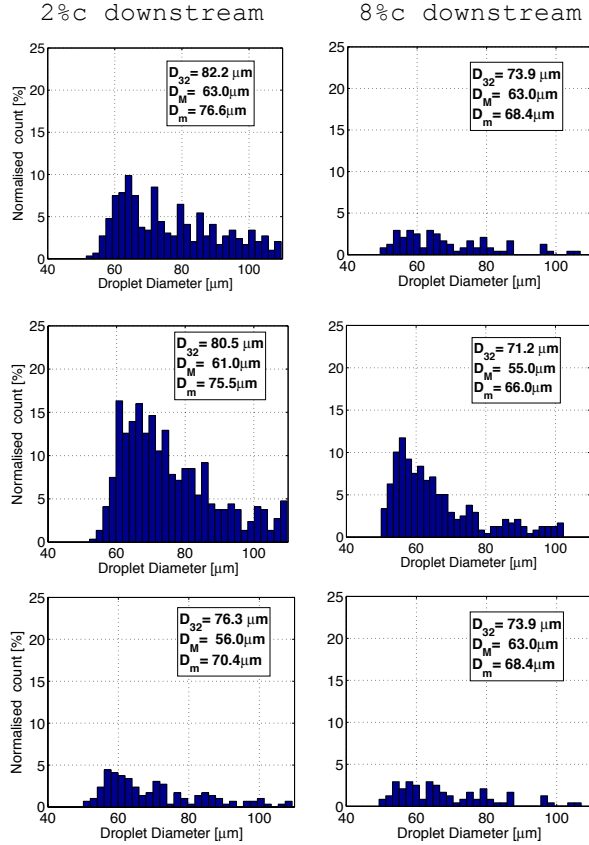


Figure 13: Size droplet distribution at tip (upper), midspan (center) and hub(bottom) spanwise locations for part load condition at x/c 2% and 8% downstream of stator 1 exit

As described above the velocity and the droplet size are the two main parameters affecting the erosion process at rotor leading edge. Therefore, in order to verify the size of the droplets at the time when they impact the rotor leading edge the weber number as a function of droplet diameter is presented in Figure 14 for the midspan location. Similar results were obtained for the tip and hub regions. Measurements at 8%c downstream of stator 1 show that the weber number is below the critical value of 22 for all droplet diameters. This implies that the droplets have reached a stable regime and they will not break up into smaller diameters. The final distributions are those depicted in Figure 13 (8%c

downstream) and the Sauter Mean Diameter is 73.9 μm , 71.2 μm and 73.9 μm for the tip, mid and hub span locations respectively.

The droplet speed results for the two downstream locations are presented in Figure 15.a and b. As shown in Figure 15.a the droplets accelerate by 10% for the range of 50 μm in diameter and by 40% for the large range of 100 μm . Using the same assumptions as described in Figure 11, the relative droplet diameter is calculated and plotted in Figure 15.b. The relative droplets' speed is about 105% of relative flowfield velocity and roughly constant for all droplet sizes from 45 up to 110 μm in diameter. Having measured the current droplet speeds and diameter, according to the power law equation $R_e \sim U^n$ the erosion rate at part load condition is increased exponentially and can reach 16 up to 32 times higher depending on the blade material.

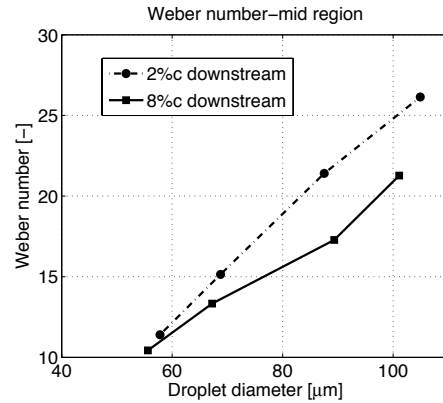


Figure 14: Weber number as a function of droplet diameter for the two different downstream axial locations of Stator 1

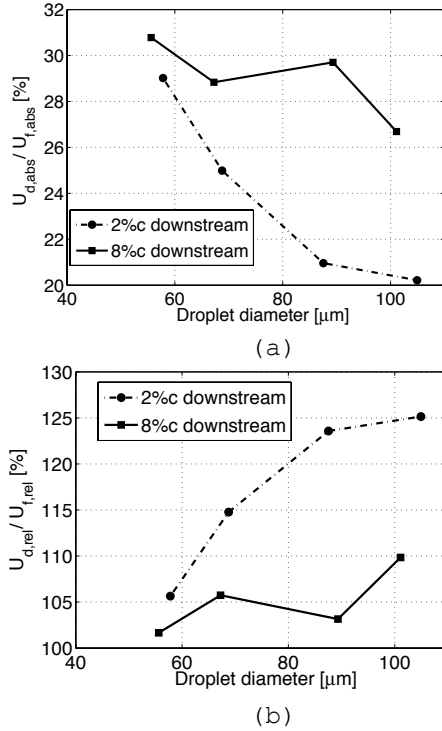
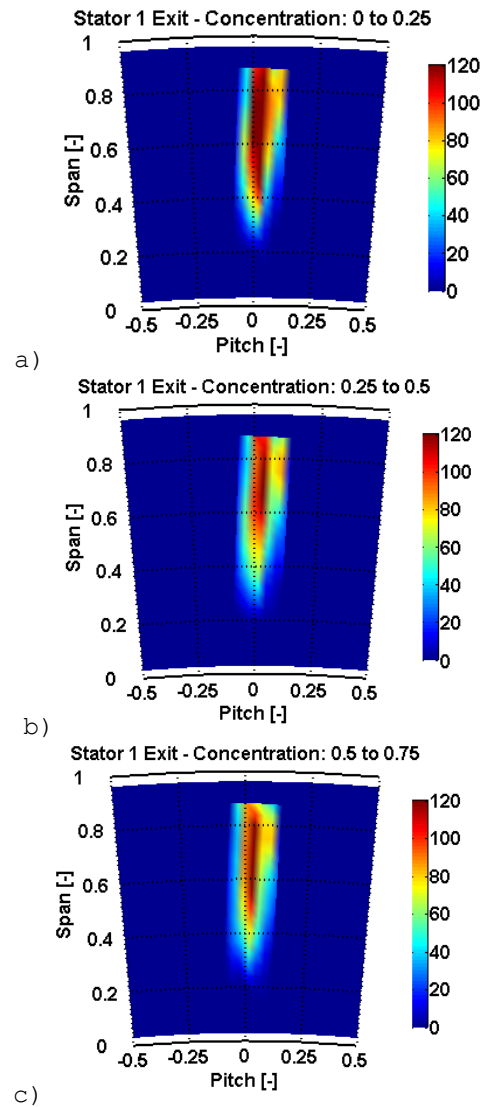


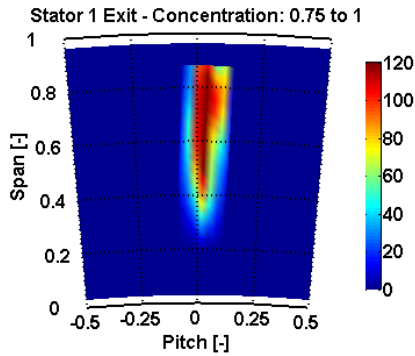
Figure 15: Absolute (a) and relative (b) droplet velocity at midspan location at $x/c=2\%$ and 8% for part load condition

Time resolved results for design condition at $x/c=2\%$

The time-resolved droplet concentration downstream of stator 1 are presented and discussed in the current paragraph. Figure 16 shows contour plots of droplets count distribution at the exit plane of stator 1 over 4 rotor blade passing sub-periods equal to $t/T = 0.25$, where T is the respective rotor blade passing time period. It can be seen that the droplets count distribution is modulated over a rotor blading passing period due to the flow field periodical interaction with the downstream rotor potential field as reported by Behr et al. [13]. At $t/T=0$ the rate gets its maximum value of almost 120drops/rev from 30% up to 90% span covering 20% of the stator pitch. At time $t/T=0.25$ the droplet rate is reduced by 23% and as consequence the actual area that the droplets cover is reduced

covering lower range in spanwise and pitchwise direction. At $t/T=0.5$ the droplet rate increases by 16% which again results in the same increase on the area coverage and finally at time $t/T=0.75$ the droplet rate exhibits a similar distribution then at $t/T=0$. This implies that the potential field of the rotor blade as it crosses the stator trailing edge generates a periodical fluctuation in droplet impact rate with a variation of 15% around the mean value of 100drops/rev.





d)

Figure 16: Time resolved droplet rate [droplets/rev] at Stator 1 exit plane for design point at four instants of the rotor blade passing period: a) $t/T=0.00$; b) $t/T=0.25$, c) $t/T=0.50$ and d) $t/T=0.75$

Conclusions

- A novel optical backscatter probe for particle measurements in the flow path of a gas turbine was demonstrated at the stator exit of an axial turbine equipped with a water droplet spray generator.
- The coarse droplets ($D_d > 45 \mu\text{m}$) count is found to be maximum at the stator's trailing edge. This is due to the impact of the droplets at stator's pressure side and the formation of a water film which is periodically torn apart from the trailing edge.
- Measurements have shown that the droplets increase by 10% in size when the flow velocity is reduced from $Ma=0.52$ to $Ma=0.42$ due to significant reduction on the shear forces between the droplets and the stream flow.
- The variation on the absolute flow velocity among the blade span from hub tip, results on 10% variations on the droplet Sauter mean diameter. Droplet speed measurements have shown that the coarse droplets suffer from a deficit in absolute velocity at the stator exit and will therefore impact the downstream rotor leading edge on the suction side. In addition,

the part load condition results in an increase of the relative droplet velocity by 40% compared to the design operating point, and as a consequence the erosion rate can increase up to 32 times depending on the material used for the rotor blade.

- The time-resolved coarse droplet count distribution at stator 1 exit plane has shown that the droplet concentration is triggered by the interaction with the downstream rotor potential field. In the current axial turbine, the rotor potential field induces up to 15% periodical fluctuation in droplet generation rate.

Acknowledgements

The authors would like to thank Mitsubishi Hitachi Power Systems, and more specifically Dr. Shigeki Senoo for the financial and technical support provided in the course of the current project.

In addition the authors would like to acknowledge the support of Flori Alickaj for his contribution in the development of the FRAP-OB measurement system. Many appreciations go to Dr. Kai Regina and Rainer Schaedler for their active support during the measurement campaign in LISA facility.

References

- [1] Webb, J., Casaday, B., Barker, B., Bons, J. P., Gledhill, A. D., and Padture, N. P., 2012, "Coal Ash Deposition on Nozzle Guide Vanes-Part I: Experimental Characteristics of Four Coal Ash Types," *Journal of Turbomachinery*, 135(2), p. 021033.
- [2] Laycock, R. G. and Fletcher, T. H., 2012, "Time-Dependent Deposition Characteristics of Fine Coal Fly Ash in a Laboratory Gas Turbine

- Environment," *Journal of Turbomachinery*, 135(2), p. 021003.
- [3] Villora, N., Dullenkopf, K., and Bauer, H., "Separation of Particles in the Secondary Air System of Gas Turbines," presented at the Volume 1: Aircraft Engine; Ceramics; Coal, Biomass and Alternative Fuels; Wind Turbine Technology, 2011.
- [4] Reema, K., Prasad, J. V. R., Rajkeshar, S., Swati, S., Andy, B.-S., and Tsuguji, N., 2014, "Modeling and Analysis of Ice Shed in Multistage Compressor of Jet Engines," *6th AIAA Atmospheric and Space Environments Conference*,
- [5] Mason, J. G., Chow, P., and Fuleki, D. M., 2010, "Understanding Ice Crystal Accretion and Shedding Phenomenon in Jet Engines Using a Rig Test," *Journal of Engineering for Gas Turbines and Power*, 133(4), pp. 041201-041201.
- [6] Venkataramani, K., Plybon, R., Raymond, H., and Brian, K., 2008, "Aircraft Engine Icing Model," *46th AIAA Aerospace Sciences Meeting and Exhibit*,
- [7] Xavier, V., Wagdi, H., Martin, A., and Guido, B., "FENSAP-ICE: Ice Accretion in Multi-Stage Jet Engines," in *19th AIAA Computational Fluid Dynamics*, ed: American Institute of Aeronautics and Astronautics, 2009.
- [8] White, A. J. and Meacock, A. J., 2004, "An Evaluation of the Effects of Water Injection on Compressor Performance," *Journal of Engineering for Gas Turbines and Power*, 126(4), pp. 748-754.
- [9] Obermüller, M., Schmidt, K.-J., Schulte, H., and Peitsch, D., 2012, "SOME ASPECTS ON WET COMPRESSION - PHYSICAL EFFECTS AND MODELING STRATEGIES USED IN ENGINE PERFORMANCE TOOLS," *Deutscher Luft- und Raumfahrtkongress*
- [10] Sun, L., Zheng, Q., Luo, M., Li, Y., and Bhargava, R., 2010, "Understanding Behavior of Water Droplets in a Transonic Compressor Rotor With Wet Compression," *Industrial and Cogeneration; Microturbines and Small Turbomachinery; Oil and Gas Applications; Wind Turbine Technology*, 5
- [11] Bosdas, I., Mansour, M., Kalfas, A., and Abhari, R. S., 2015, "An optical backscatter probe for time resolved droplet measurements," *under submission on Measurement Science and Technology*,
- [12] Rollinger, B., Morris, O., and Abhari, R. S., 2011, "Stable tin droplets for LPP EUV sources," *Extreme Ultraviolet (EUV) Lithography II*,
- [13] Behr, T., Kalfas, A. I., and Abhari, R. S., 2007, "Unsteady Flow Physics and Performance of a One-and-1/2-Stage Unshrouded High Work Turbine," *ASME Journal of Turbomachinery*, 129, pp. 348-359.
- [14] Lee Black, D., McQuay, M. Q., and Bonin, M. P., 1996, "Laser-based techniques for particle-size measurement: A review of sizing methods and their industrial applications," *Progress in Energy and Combustion Science*, 22(3), pp. 267-306.
- [15] Ow, C. S. and Crane, R. I., 1979, "On the Critical Weber Number for Coarse Water Formation in Steam Turbines," *Journal of Mechanical Engineering Science*, 21(5), pp. 353-356.
- [16] Cai, X., Ning, D., Yu, J., Li, J., Ma, L., Tian, C., et al., 2014, "Coarse water in low-pressure steam turbines," *Proceedings of the*

- Institution of Mechanical Engineers, Part A: Journal of Power and Energy*, 228(2), pp. 153-167.
- [17] Ahmad, M., Casey, M., and Sürken, N., 2009, "Experimental assessment of droplet impact erosion resistance of steam turbine blade materials," *Wear*, 267(9-10), pp. 1605-1618.
- [18] Lam, T. C. T. and Dewey, R., 2003, "A Study of Droplet Erosion on Two L-0 Turbine Stages," International Joint Power Generation Conference, Atlanta USA
- [19] Crane, R. I., 2004, "Droplet deposition in steam turbines," *Proceedings of the Institution of Mechanical Engineers, Part C: Journal of Mechanical Engineering Science*, 218(8), pp. 859-870.
- [20] Eisfeld, T. and Joos, F., "Experimental Investigation of Two-Phase Flow Phenomena in Transonic Compressor Cascades," presented at the Volume 7: Turbomachinery, Parts A and B, 2009.